J. Fluid Mech. (1970), *vol.* 44, *part* 3, *pp.* 493–512
Printed in Great Britain

Numerical study of steady flow past spheroids

By JACOB H. MASLIYAH AND NORMAN EPSTEIN
Department of Chemical Engineering, University of British Columbia

(Received 3 July 1969 and in revised form 7 July 1970)

Numerical methods have been used to investigate the steady incompressible flow past oblate and prolate spheroids for Reynolds numbers up to 100. The ratio of minor to major axis of the spheroids investigated were 0·9, 0·5 and 0·2, together with 1·0, which represents the limiting case of a sphere. The pressure distribution and the skin and form drag coefficients were numerically evaluated for the various Reynolds numbers. Streamlines, equi-vorticity lines and equi-velocity lines are presented and show in detail the flow characteristics.

1. Introduction

The study of isothermal steady laminar flow of an incompressible Newtonian fluid past a rigid body requires the solution of the Navier–Stokes equation and the equation of continuity, subject to the prevailing boundary conditions. The Navier–Stokes equation, being non-linear, has so far proved insoluble for the problem of axisymmetric flow around oblate and prolate spheroids (a sphere and a disk being limiting forms of an oblate spheroid), except by techniques which linearize the equations of motion by approximations. Such solutions are given by Stokes (1851), Oseen (1910), Goldstein (1929), Tomotika & Aoi (1950), Pearcey & McHugh (1955) and Proudman & Pearson (1957) for spheres, and Sampson (1891), Aoi (1955) and Breach (1961) for spheroids.

Jenson (1959), using a finite difference method, solved the Navier–Stokes equation for the flow past a sphere at R up to 40 by splitting the fourth-order equation in the stream function into two second-order equations, after Thom (1927). Subsequently Jenson, Horton & Wearing (1968) extended this work to $R = 80$. Rhodes (1967) and LeClair & Hamielec (1968) extended Jenson's technique with the aid of digital computers to R of 100 and 1000, respectively. But their results for an isolated sphere at low R are not conclusive, inasmuch as their porosities are insufficiently high to accurately represent an infinite medium (Masliyah & Epstein 1969).

Rimon & Cheng (1969) obtained the transient uniform flow around a sphere for R up to 1000. Their results for the surface pressure distribution at 'steady state' conditions for $R = 10$ are, however, at variance with those of Pearcey & McHugh, of Jenson and of Rhodes. Rimon & Lugt (1969) arrived at the steady state solution for flow past oblate spheroids at $R = 0$ and $R = 100$ by solving the time-dependent Navier–Stokes equation.

2. Formulations

The choice of spheroidal co-ordinates in this study facilitates the formulation of the spheroidal boundary conditions and the use of a finite difference method. In addition, the exponential properties of the spheroidal co-ordinates give a fine lattice near the surface of the spheroid in general and near the tips in particular, and a coarse lattice far away from the surface. Happel & Brenner (1965) discuss spheroidal co-ordinates in detail.

Using oblate spheroidal co-ordinates (ξ, η) the Navier–Stokes equation can be written as

$$\operatorname{sech}\xi_a E^2(E^2\psi) = \frac{R}{2}\left[\frac{\cosh\xi\sin\eta}{\sinh^2\xi+\cos^2\eta}\right]\left[\frac{\partial\psi}{\partial\xi}\frac{\partial}{\partial\eta}\left(\frac{E^2\psi}{\cosh^2\xi\sin^2\eta}\right)\right.$$
$$\left.-\frac{\partial\psi}{\partial\eta}\frac{\partial}{\partial\xi}\left(\frac{E^2\psi}{\cosh^2\xi\sin^2\eta}\right)\right], \tag{1}$$

with
$$E^2 = \frac{1}{\sinh^2\xi+\cos^2\eta}\left[\frac{\partial^2}{\partial\xi^2}-\tanh\xi\frac{\partial}{\partial\xi}+\frac{\partial^2}{\partial\eta^2}-\cot\eta\frac{\partial}{\partial\eta}\right], \tag{2}$$

and
$$E^2\psi = \zeta\cosh\xi\sin\eta\operatorname{sech}^3\xi_a. \tag{3}$$

The following dimensionless quantities are used:

$$\psi = \psi'/Ua^2, \quad R = 2aU/\nu \quad \text{and} \quad \zeta = \zeta' a/U,$$

where R is the Reynolds number, U is the velocity of the undisturbed stream, ν is the kinematic viscosity of the fluid, ψ is the dimensionless stream function and ζ the dimensionless vorticity, while the primed symbols represent the corresponding dimensional quantities. The term a is the length of the major semi-axis of the spheroid, and is equal to $c\cosh\xi_a$, where ξ_a is the value of ξ at the surface of the spheroid, c being a characteristic length of the co-ordinate system.

For a spheroid which is almost spherical, $\cosh\xi$ becomes very large, and difficulty will be encountered in the numerical analysis. For this reason the following functions are introduced:

$$G = \frac{\zeta\cosh\xi\sin\eta}{\cosh\xi_a}, \tag{4}$$

and
$$F = \frac{\zeta\cosh\xi_a}{\cosh\xi\sin\eta}. \tag{5}$$

Splitting (1) into two equations, one in terms of ψ, ξ and η, and the other in terms of $E^2\psi$, ξ and η, and introducing (4) and (5), yields

$$E^2G = \frac{\operatorname{sech}\xi_a R}{2}\left[\frac{\cosh\xi\sin\eta}{\sinh^2\xi+\cos^2\eta}\right]\left[\frac{\partial\psi}{\partial\xi}\frac{\partial F}{\partial\eta}-\frac{\partial\psi}{\partial\eta}\frac{\partial F}{\partial\xi}\right], \tag{6}$$

and
$$E^2\psi = G\operatorname{sech}^2\xi_a. \tag{7}$$

The solution of the above two simultaneous differential equations in the stream function and in the modified vorticity G could be achieved by using Jenson's

relaxation technique. This technique involves approximating the differential equations by finite difference equations which relate the values of neighbouring points on a flow grid. The solution of these equations is followed by interpolation between the grid points over the whole field of influence. The details of the numerical analysis are given by Masliyah (1970).

For a prolate spheroid, the governing equations could be obtained from those of an oblate spheroid by replacing each $\sinh\xi$ by $i\cosh\xi$ and each $\cosh\xi$ by $i\sinh\xi$. By this procedure the term a will then represent the length of the minor semi-axis.

3. Boundary conditions

Although the flow is considered to be in an infinite medium, it is not possible to perform the numerical analysis in an infinite domain. The field of computation is therefore restricted by an outer spheroidal envelope which, like the spheroidal surface, coincides with one of the spheroidal co-ordinate grid lines as shown in figure 1.

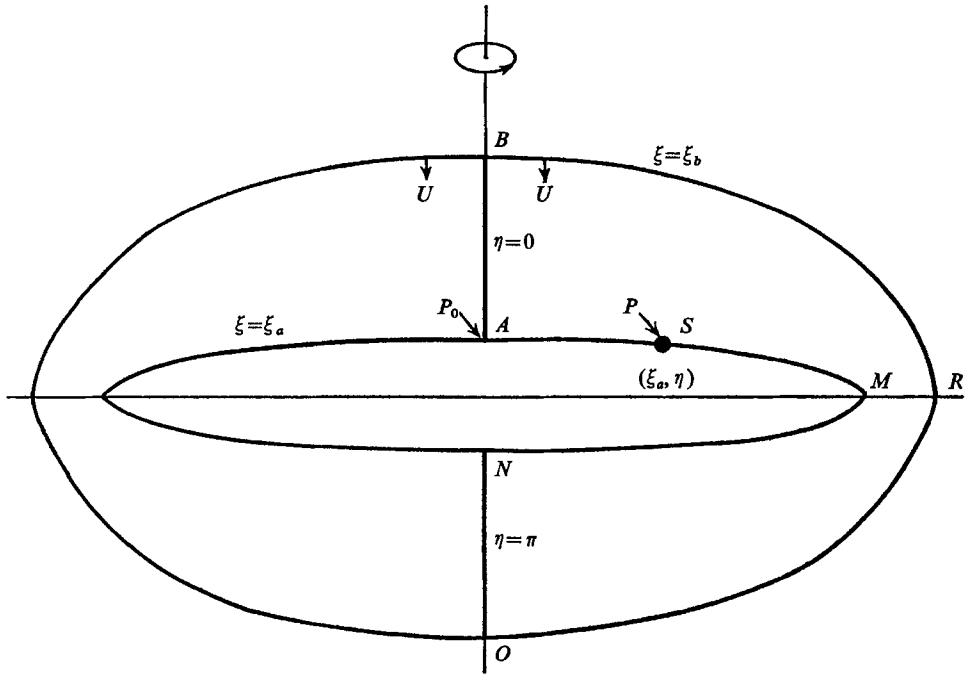

FIGURE 1. Oblate spheroid with its outer envelope.

As the two flow equations are of second order, four boundary conditions are to be satisfied. For an oblate spheroid, the boundary conditions for ψ are,

$$\left.\begin{array}{llll} \text{for} & \eta = 0, & \text{along } BA, & \psi = 0, \\ & \eta = \pi, & \text{along } NO, & \psi = 0, \end{array}\right\} \text{axis of symmetry,}$$

$$\xi = \xi_a, \quad \text{along } AMN, \quad \psi = 0 \quad \text{(surface of spheroid).}$$

At the outer boundary, $\xi = \xi_b$, the flow is assumed to be a streaming parallel flow, giving

$$\psi = \tfrac{1}{2}\sin^2\eta\cosh^2\xi_b\,\mathrm{sech}^2\xi_a.$$

The boundary conditions for ζ are,

$$\begin{aligned}
&\text{for}\quad \eta = 0, \quad \text{along } BA, \quad \zeta = 0,\\
&\qquad \eta = \pi, \quad \text{along } NO, \quad \zeta = 0,\\
&\qquad \xi = \xi_b, \quad \text{along } BRO, \quad \zeta = 0 \quad \text{(outer boundary)},\\
&\qquad \xi = \xi_a, \quad \text{along } AMN, \quad \zeta = \frac{E^2\psi\cosh^2\xi_a}{\sin\eta}.
\end{aligned}$$

The last boundary condition for vorticity could be written in finite difference form by assuming the no-slip condition at the surface of the spheroid, and by expanding $E^2\psi$ using Taylor's series expansions correct to the third order. Again, the boundary conditions for a prolate spheroid could be obtained by replacing $\sinh\xi$ with $i\cosh\xi$ and $\cosh\xi$ by $i\sinh\xi$.

4. Pressure distribution and drag coefficients

The drag on a body is usually expressed in terms of a dimensionless drag coefficient,

$$C_D = \frac{\text{drag force in the flow direction}}{\text{projected area normal to the direction of flow} \times \text{kinetic pressure}}.$$

The skin drag coefficient is given by

$$C_{DS} = \frac{8}{R}\tanh\xi_a\int_0^{\pi}\sin^2\eta\;\zeta_a\,d\eta. \tag{8}$$

In the limiting case of a sphere, $\tanh\xi_a$ is unity, and equation (8) becomes identical to that given by Jenson for a perfect sphere. For an infinitesimally thin circular disk, $\tanh\xi_a$ is zero, and thus (8) shows a zero skin drag coefficient, in conformity with simple geometrical considerations.

Referring to figure 1, the pressure distribution around the oblate spheroid is given by

$$P - P_0 = \frac{4}{R}\int_0^{\eta}\left(\left.\frac{\partial\zeta}{\partial\xi}\right|_{\xi=\xi_a} + \zeta_a\tanh\xi_a\right)d\eta, \tag{9}$$

where the dimensional pressure p' was rendered dimensionless by putting

$$P = p' - p'_{st}/(\tfrac{1}{2}\rho U^2),$$

p'_{st} being the static pressure. The dimensionless frontal stagnation pressure, P_0, is given by

$$P_0 = 1 + \frac{8}{R}\int_{\xi_a}^{\xi_b}\left.\frac{\partial\zeta}{\partial\eta}\right|_{\eta=0}d\xi. \tag{10}$$

The form or pressure drag coefficient is then given by

$$C_{DF} = \int_0^{\pi} P\sin 2\eta\,d\eta. \tag{11}$$

The total drag coefficient is obtained by adding the skin and form drag coefficients. The corresponding equations for a prolate spheroid could be derived by the usual transformation.

5. Low Reynolds number flow

The flow equation in terms of the stream function for an oblate spheroid at $R = 0$ becomes $E^4\psi = 0$, where

$$E^2 = \frac{1}{\lambda^2+\theta^2}\left[(\lambda^2+1)\frac{\partial^2}{\partial\lambda^2}+(1-\theta^2)\frac{\partial^2}{\partial\theta^2}\right],$$

and $\lambda = \sinh\xi$, $\theta = \cos\eta$. For the boundary conditions of no slip at the surface of the spheroid, and streaming flow and zero vorticity at the outer envelope, the above flow equation has no closed separable solution when the outer envelope is at a finite distance from the spheroid. This conclusion, which could be derived by carefully examining Sampson's solution, was also obtained by O'Brien (1961).

For the flow past a spheroid in an infinite medium, the Stokes solution gives the following total drag coefficient:

$$C_{\mathrm{DT}} = 24K/R, \tag{12}$$

where

$$K_{\mathrm{oblate}} = 1/[\tfrac{3}{4}(\lambda_a^2+1)^{\frac{1}{2}}[\lambda_a-(\lambda_a^2-1)\cot^{-1}\lambda_a]] \tag{13}$$

$$K_{\mathrm{prolate}} = 1/[\tfrac{3}{4}(\tau_a^2-1)^{\frac{1}{2}}[(\tau_a^2+1)\coth^{-1}\tau_a-\tau_a]] \tag{14}$$

and $\tau_a = \cosh\xi_a$, the subscript a denoting the surface of the spheroid.

The expression given by Oseen (1927) and Aoi could be written as

$$C_{\mathrm{DT}} = \frac{24K}{R}\left[1+\frac{3KR}{16}\right]. \tag{15}$$

Breach's expression, after some transformation, becomes

$$C_{\mathrm{DT}} = \frac{24K}{R}\left[1+\frac{3KR}{16}+\frac{9K^2}{160}R^2\ln\left(\frac{R}{2}\right)\right]. \tag{16}$$

The above expressions for the total drag coefficients show clearly the deviation of an oblate and a prolate spheroid from a sphere with the same equatorial diameter. For a sphere, $K = 1$, and (12), (15) and (16) reduce to the well-known Stokes, Oseen and Proudman & Pearson expressions, respectively. Despite a misprint in their expression for K_{oblate}, Happel & Brenner provide an accurate tabulation of K as a function of aspect ratio for both oblate and prolate spheroids. For a thin circular disk (A.R. = 0), the tabulated value of K is 0·84883.

The dimensionless surface pressure distribution for the Stokes flow past an oblate spheroid is

$$P = 1+\frac{6K_{\mathrm{oblate}}}{R}\left[\frac{\lambda_a^2+1}{\lambda_a^2+\cos^2\eta}\right]\cos\eta, \tag{17}$$

and, for a prolate spheroid,

$$P = 1 + \frac{6K_{\text{prolate}}}{R}\left[\frac{\lambda_a^2}{\lambda_a^2 + \sin^2\eta}\right]\cos\eta. \tag{18}$$

For a sphere, $K \to 1$, $\lambda_a \to \infty$, and (17) and (18) both become

$$P = 1 + (6/R)\cos\eta. \tag{19}$$

When $R \to 0$, P becomes anti-symmetric about $\eta = \frac{1}{2}\pi$.

The ratio $C_{\text{DF}}/C_{\text{DS}}$ for a prolate, and $C_{\text{DS}}/C_{\text{DF}}$ for an oblate, spheroid from Oseen's expansion as given by Aoi are respectively

$$C_{\text{DF}}/C_{\text{DS}} = \frac{(\tau_a^2 - 1)(\tau_a \coth^{-1}\tau_a - 1)}{1 - (\tau_a^2 - 1)(\tau_a \coth^{-1}\tau_a - 1)}, \tag{20}$$

and

$$C_{\text{DS}}/C_{\text{DF}} = \frac{1 - (\lambda_a^2 + 1)(1 - \lambda_a \cot^{-1}\lambda_a)}{(\lambda_a^2 + 1)(1 - \lambda_a \cot^{-1}\lambda_a)}. \tag{21}$$

According to the above equations, the drag coefficient ratios are independent of R.

6. Validity of the finite difference solution

In the relaxation procedure, misleading results could be obtained from the values of the field functions at the lattice points unless great care were taken by considering the various computational parameters that could influence the flow field. These parameters are: (i) the number of Taylor expansion terms used, (ii) convergence tolerance, (iii) mesh size, (iv) position of the outer boundary, and (v) the differentiation technique. Comments on each parameter follow.

(i) The flow equations were transformed to finite difference equations by using second-order Taylor expansions. Jenson, in his work on spheres, used both second- and fourth-order Taylor expansions for $R = 5$, and found no difference in the accuracy of the final values of the drag coefficients for a lattice spacing of 12° in the angular, and 0·2 unit of $\ln r$ (where r = dimensionless, radial co-ordinate) in the radial, direction. Although a similar insensitivity to the order of the Taylor expansion would be less probable for a spheroid of small aspect ratio, the second-order expansion was nevertheless used throughout this analysis, in order to keep the computer time within reasonable bounds.

(ii) Convergence of the computed values for the stream function and vorticity was assumed when no further change was apparent in the fourth significant figure of any function between successive iterations. With such a tolerance, the drag coefficients and surface pressure distributions would not change by more than 0·2 and 0·5 %, respectively, for a further 50 iterations. During the course of this work it was found that, while the drag coefficients were not very sensitive to the degree of convergence of the lattice points, $P_{\eta=\pi}$ was very sensitive to the degree of convergence.

(iii) The effect of the mesh size for the oblate spheroids at $R = 50$ and $R = 100$ was evaluated by changing the grid size for the angle from $\simeq 6°$ to $\simeq 3°$, and the

radial step from $\simeq 0{\cdot}06$ to $\simeq 0{\cdot}03$. The resulting change in the total drag coefficients for the two Reynolds numbers at any aspect ratio was less than 1 and 2%, respectively. No change in the dimensionless frontal stagnation pressure was detected, but the rear stagnation pressure was altered by about 30%, which, however, represented only a 5% change relative to the frontal stagnation pressure. For lower R, the larger step size was used, because the rate of change of the flow functions with step size was not as rapid as that for higher values of R. The shape of the wake was found not to be different for the two mesh sizes used. For the prolate spheroids, the step size was found to be more critical, and therefore a smaller step size was used throughout. A change in step size of $\simeq 6°$ in the angular and $\simeq 0{\cdot}04$ in the radial direction to $\simeq 3°$ and $\simeq 0{\cdot}02$, respectively, for $R = 100$ and A.R.† $= 0{\cdot}5$, gave a 4% difference in the total drag coefficient, using the same differentiation and integration formulae. P_0 was simultaneously changed by 1% and $P_{\eta=\pi}$ by about 6% relative to P_0.

(iv) For numerical analysis purposes, the field of computation must be restricted within an outer spheroidal envelope, the position of which poses an important factor in the numerical results. The analytical solution of the creeping flow equations for a sphere surrounded by an outer spherical envelope under the boundary conditions of the present study results in a total drag coefficient, which is given by

$$C_{\mathrm{DT}} = \frac{120}{R}\left[\frac{1}{5-9\gamma+5\gamma^3-\gamma^6}\right],$$

where γ is the diameter ratio of solid sphere to spherical envelope.‡ Then

$$\frac{C_{\mathrm{DT}}|_{\gamma=0{\cdot}01}}{C_{\mathrm{DT}}|_{\gamma=0}} = 1{\cdot}018.$$

This indicates that even when the outer envelope is located at 100 diameters from the sphere, its influence on the drag coefficient is still perceptible. The drag coefficients at $R = 1{\cdot}0$ for both oblate and prolate spheroids were extrapolated to infinite envelope volume from a plot of C_{DT} against the reciprocal of the mean diameter d_m, defined as the total volume of the outer envelope divided by the volume of the spheroid, all raised to the power one-third. The range of d_m actually computed was 17–102, as shown in figure 2. At $R = 10$ the difference between the computed values of the drag coefficients for d_m of 17 and 30 was negligible for both the oblate and the prolate spheroids. For higher R, the values of d_m used to represent an infinite medium were 15 and 17 for prolate and oblate spheroids, respectively. At these values of d_m, the value of P at the outer envelope did not exceed $0{\cdot}05$, which is a measure of the error imposed by the presence of the outer envelope.

(v) The evaluation of the pressure distribution, as given by (9) and (10), involved both differentiation and integration. The latter posed no difficulty, and

† Ratio of minor to major axis of the spheroid.

‡ The expression for the drag coefficient has been arrived at by summing the shear stress and the pressure at the surface of the sphere. However, Kuwabara (1959), using the same boundary conditions, obtained a different expression for C_{DT} by evaluating the drag coefficient from the energy dissipation, the difference being due to the energy loss at the outer envelope, which becomes negligible for the low values of γ used in the present study.

it was found that Simpson's rule (3 points) and Boole's rule (5 points) gave almost identical results. On the other hand, numerical differentiation could give an uncertainty in the computed values of P, and consequently in the form drag coefficient. In order to examine the stability of the differentiation, Lagrange differentiation formulae for 3, 4 and 5 points were used. In general, for an oblate spheroid, the variation in the computed values of C_{DF} was within 0·5 %. For a

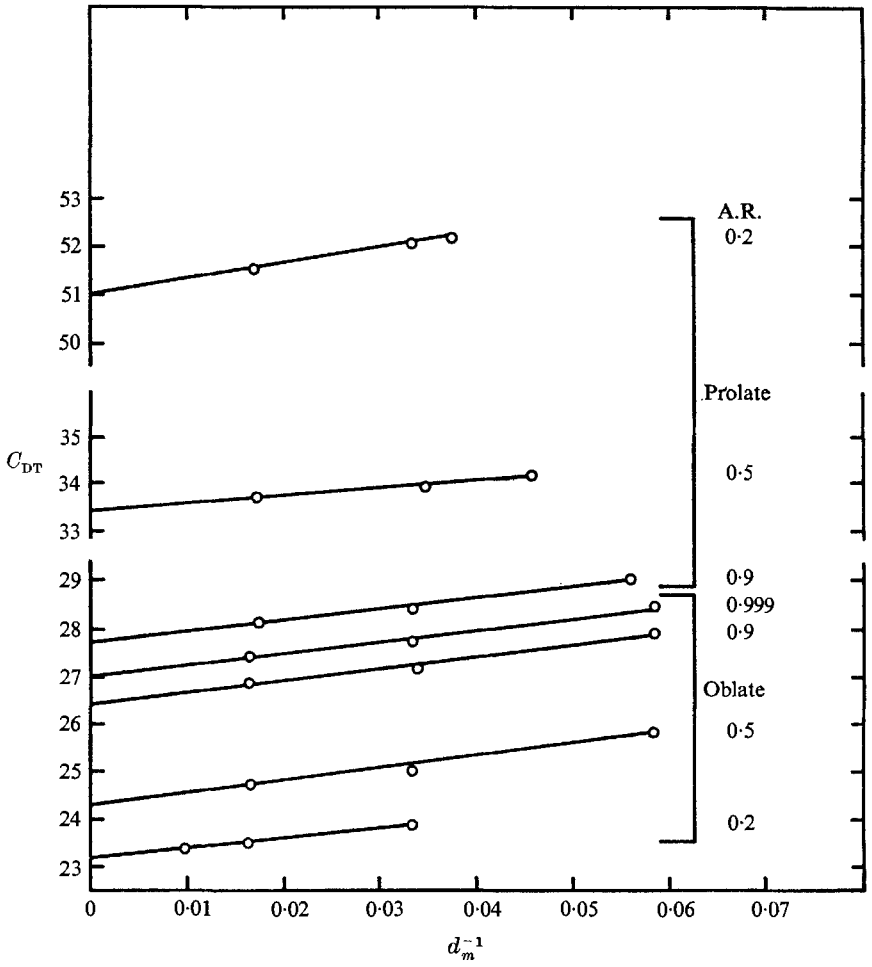

FIGURE 2. Variation of total drag coefficient with the position of the outer envelope for $R = 1{\cdot}0$.

prolate spheroid, however, difficulty was encountered, C_{DF} varying as much as 20 % for an aspect ratio of 0·2. An examination of (9) and its numerical evaluation indicates that the value of $\partial\zeta/\partial\xi|_{\xi=\xi_a}$ at low aspect ratio is negative and nearly equal to $\zeta_a \tanh \xi_a$, except near the tips of the spheroid, resulting in the flatness of the surface pressure distribution for A.R. = 0·2 shown in figures 9 and 11. This gave rise to a large error in the computed value of P and hence C_{DF}. Fortunately, for the small aspect ratios, the major contribution to C_{DT} is from the skin drag coefficient, which could be obtained with good accuracy. For $R = 1$,

and A.R. = 0·2 and 0·5, the Lagrange 5-point differentiation formula as compared to the 3-point formula gave a value of C_{DF}/C_{DS} closer to that given by (20). For higher R, only the 5-point formula was used.

7. Numerical results

For an aspect ratio of unity, the spheroid becomes a perfect sphere. In this study, an oblate spheroid with A.R. of 0·999 was considered to be a sphere. The variation of the total drag coefficient with R obtained for the limiting case of a sphere is shown in figure 3. The present computed results agree well with the experimental values summarized by Lapple & Shepherd (1940). The reason that the computed values of C_{DT} in general are above the experimental curve seems mainly to be that the outer envelope was not taken far enough for its influence to be negligible. The same direction of influence would be expected from the presence of walls confining the flow field.

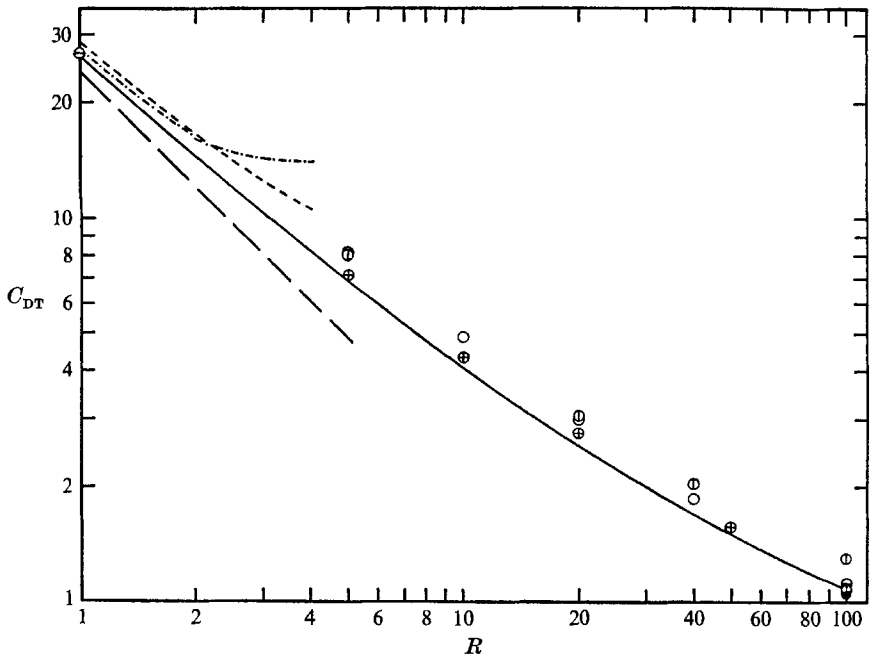

FIGURE 3. Variation of total drag coefficient with Reynolds number for a sphere. ——, Lapple & Shepherd (experimental); – – – –, Oseen; –·–·–·–·–, Proudman & Pearson; — — —, Stokes; ⊕, this study; ○, Jenson; ⊙, Rhodes; ⊖, LeClair & Hamielec; ●, Rimon & Lugt.

The variation of the total drag coefficient with Reynolds number of an oblate spheroid having various aspect ratios is given in figure 4. At low R, an oblate spheroid with higher A.R. gives a higher drag coefficient, i.e., C_{DT} for a sphere is higher than that for a circular disk. For higher R, this tendency is eventually reversed, and a spheroid with lower A.R. gives a higher C_{DT}. At low R, for which the contribution of C_{DS} to C_{DT} is large, this result appears to be quite reasonable,

since at a fixed value of R all the spheroids may be considered to have the same equatorial diameter (for constant U and ν), and consequently the surface area, and hence the skin drag coefficient, increases with A.R. For higher values of R the wake bubble becomes much larger for an oblate spheroid as A.R. decreases; and, since normally high form drag coefficients are associated with large wakes, and increasing R increases the relative contribution of C_{DF} to C_{DT}, the result is that, at sufficiently high R, C_{DT} for a low aspect ratio is higher than that for a sphere. Experimental work on disks by Schmiedel (1928) indicates that the C_{DT}–R

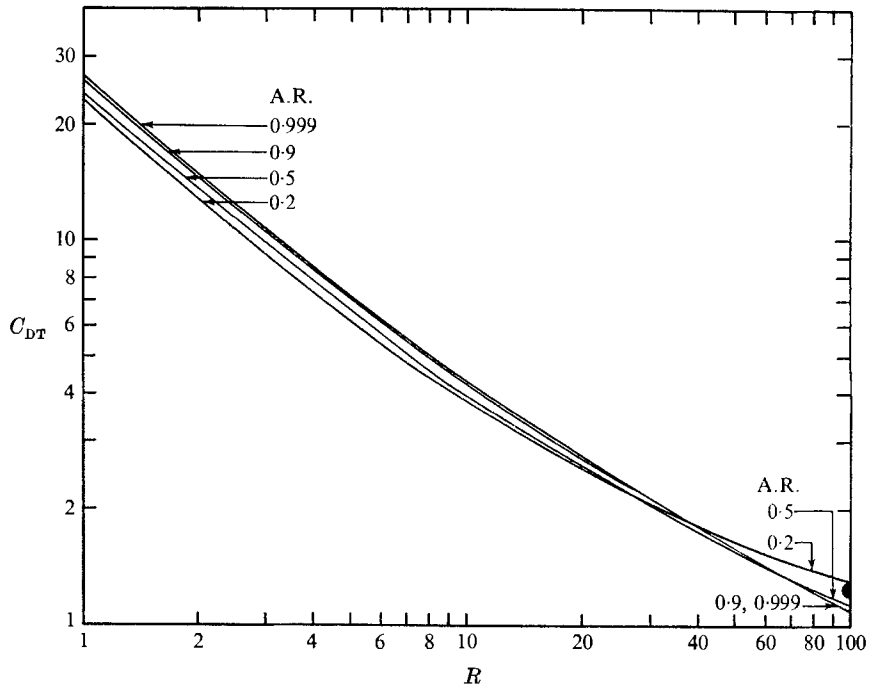

FIGURE 4. Variation of total drag coefficient with Reynolds number for various aspect ratios of an oblate spheroid. ◖ , Rimon & Lugt, A.R. = 0·2.

curve for a disk crosses that of a sphere at $R \simeq 50$. A disk may be thought of as the limiting oblate spheroid of zero aspect ratio. The total drag coefficient given by Rimon & Lugt for A.R. = 0·2 at $R = 100$ is in agreement with the present work.

Figure 5 shows the variation of C_{DT} with R for various aspect ratios of a prolate spheroid. The comparison at a fixed value of R may once again be considered as based on spheroids having the same equatorial diameter for fixed U and ν.

The ratio of skin to form drag coefficient for oblate spheroids at different Reynolds numbers is shown in figure 6 as a function of aspect ratio. At $R = 1{\cdot}0$, Aoi's expression, as given by (21), is in good agreement with the present numerical study. The relative contribution of C_{DS} to C_{DT} decreases with R for all aspect ratios. The same is observed for prolate spheroids as given by the plot of C_{DF}/C_{DS} *vs.* A.R. in figure 7. Aoi's expression, (20), is again in good agreement at $R = 1{\cdot}0$.

However, the relative contribution of C_{DS} to C_{DT} increases with A.R. for an oblate, but decreases for a prolate, spheroid.

The dimensionless pressure distribution at the surface of an oblate spheroid for different A.R. is shown in figure 8 for $R = 1{\cdot}0$. The Stokes pressure distributions for both a sphere and an oblate spheroid with A.R. = 0·2 are in good agreement with the computed distributions, considering that even for a sphere the Stokes régime is strictly valid only for $R \leqslant 0{\cdot}1$. It is interesting to note sharp maxima and minima for A.R. = 0·2, less pronounced ones for A.R. = 0·5, and none at all

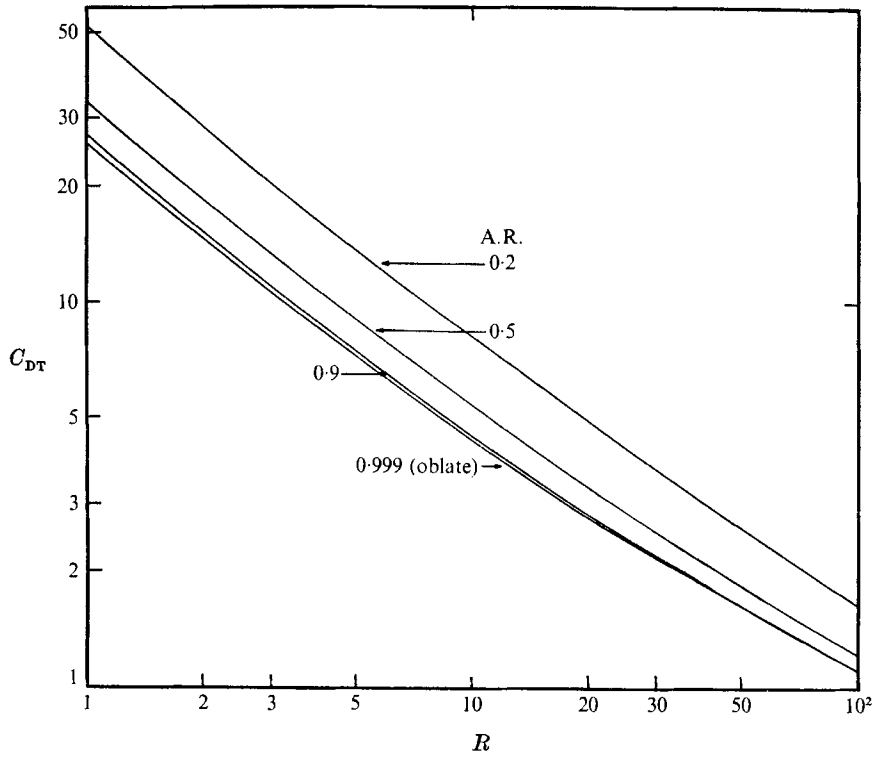

FIGURE 5. Variation of total drag coefficient with Reynolds number for various aspect ratios of a prolate spheroid.

for A.R. of 0·9. The exact value of A.R. where maxima and minima would be obliterated for the Stokes flow could be found from (17). The dimensionless surface pressure distribution on a prolate spheroid with different A.R. is given in figure 9 for $R = 1{\cdot}0$. A comparison with the Stokes pressure distribution for A.R. = 0·2 shows general agreement in the shape of the curve, but a considerable difference in the frontal stagnation pressure. For $R = 100$, the surface pressure distributions for the oblate and prolate spheroids are given in figures 10 and 11, respectively. For an oblate spheroid with A.R. = 0·2 the pressure increases rapidly just before the boundary-layer separation point, whereas for the same A.R. for a prolate spheroid the pressure increases slowly and no separation is observed. For a nearly perfect sphere (A.R. = 0·999), the surface pressure distribution is in excellent agreement with that of a perfect sphere, given by

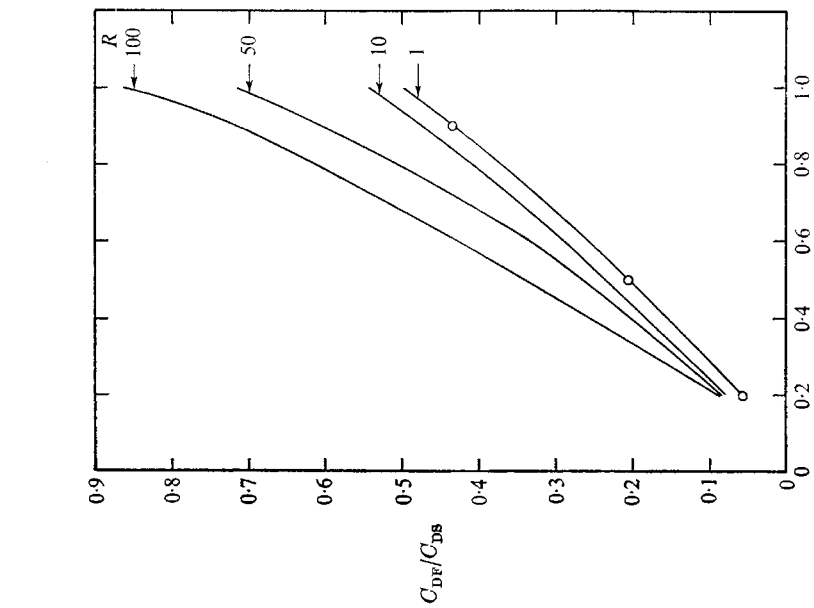

FIGURE 7. Form to skin drag coefficient ratio variation with aspect ratio for prolate spheroids; ——, this study; ○, Aoi.

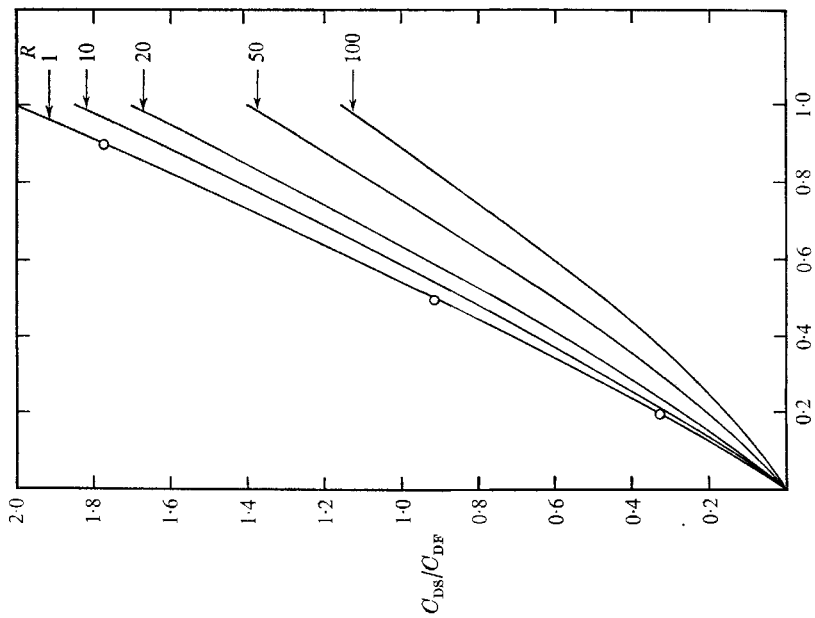

FIGURE 6. Skin to form drag coefficient ratio variation with aspect ratio for oblate spheroids; ——, this study; ○, Aoi.

Hamielec, Hoffman & Ross (1967). However, the pressure distributions given by Rimon & Lugt for A.R. = 1 (sphere) and A.R. = 0·2 tend to deviate from the present work at the rear end of the particles, as shown in figure 10. This might be due to steady-state conditions not being fully reached by the transient approach of Rimon & Lugt.

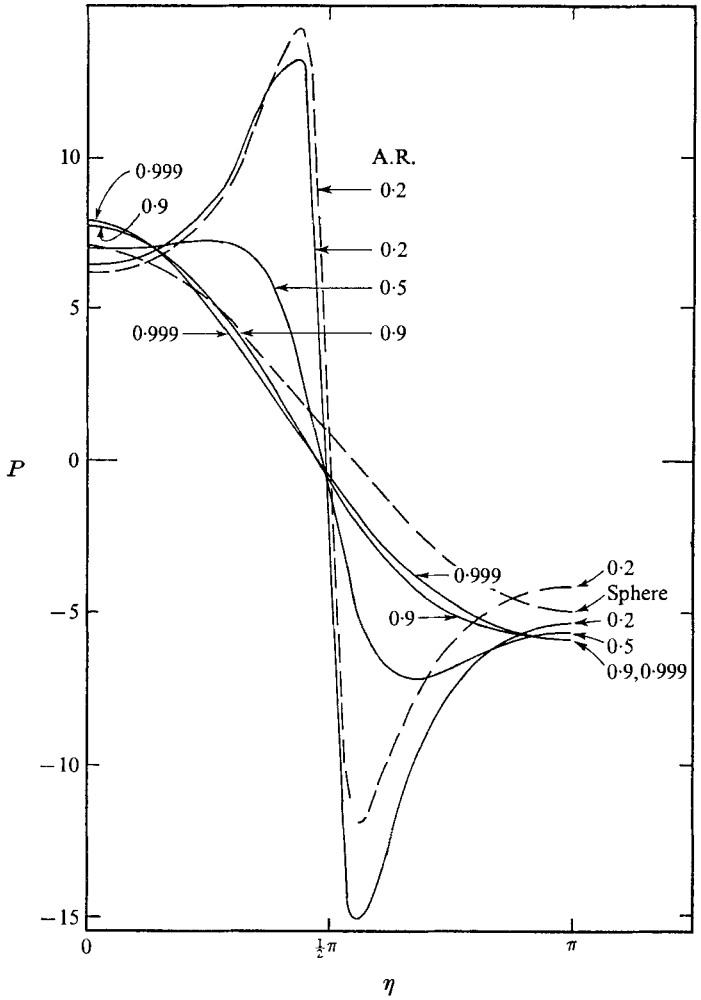

FIGURE 8. Dimensionless surface pressure distribution for various aspect ratios of an oblate spheroid at $R = 1{\cdot}0$. – – – –, Stokes.

It is interesting that the frontal stagnation pressure for the various aspect ratios of both oblate and prolate spheroids differ considerably from each other, P_0 for an oblate spheroid with A.R. = 0·2 being closest to unity at both $R = 1{\cdot}0$ and $R = 100$. Moreover, this deviation from unity increases with decreasing Reynolds number. This seems to confirm two well-observed characteristics of static Pitot tubes, namely, that the correction factor is large for low R and that it varies considerably for different tip shapes (Folsom & Arbor 1956).

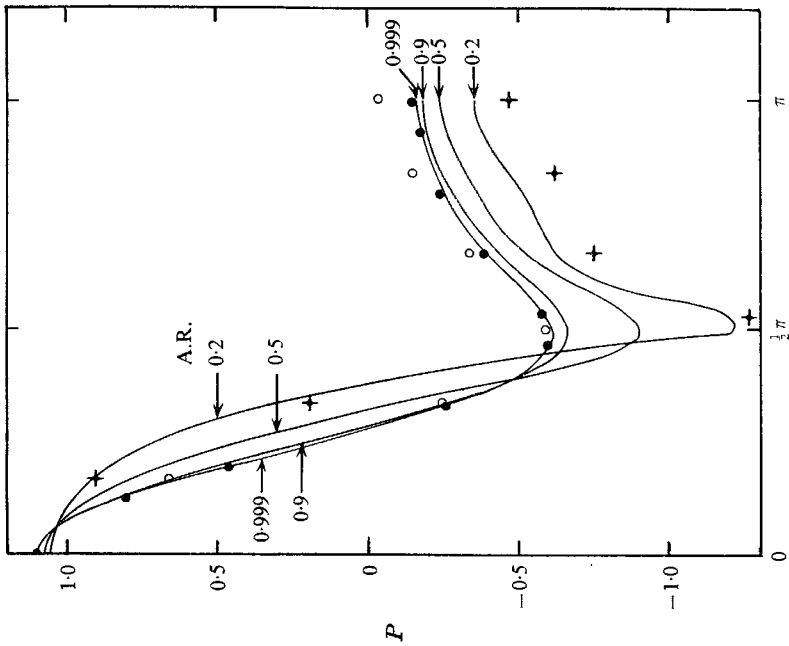

FIGURE 10. Dimensionless surface pressure distribution for various aspect ratios of an oblate spheroid at $R = 100$; ——, this study; ●, Hamielec *et al.*, perfect sphere; ○, Rimon & Lugt, perfect sphere; +, Rimon & Lugt, A.R. = 0·2.

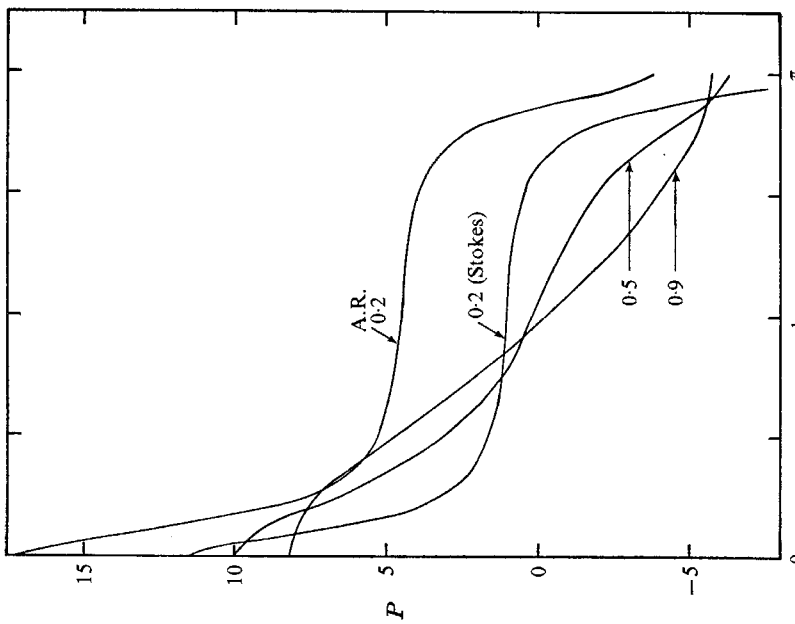

FIGURE 9. Dimensionless surface pressure distribution for various aspect ratios of a prolate spheroid at $R = 1·0$.

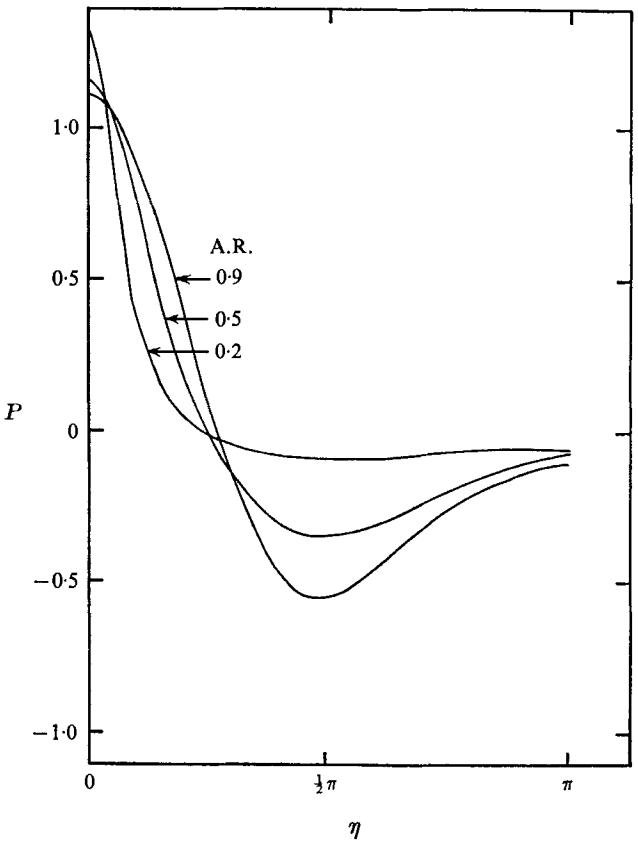

FIGURE 11. Dimensionless surface pressure distribution for various aspect ratios of a prolate spheroid at $R = 100$.

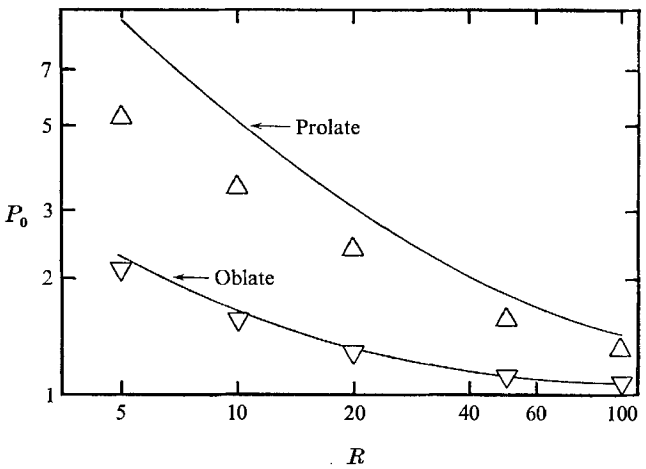

FIGURE 12. Variation of the dimensionless frontal stagnation pressure with Reynolds number for A.R. = 0·2; ——, boundary-layer theory; △, prolate spheroid (this study); ▽, oblate spheroid (this study).

At high Reynolds numbers, Homann's (1936) boundary-layer formula for the frontal stagnation point is

$$P_0 = 1 + \frac{A}{R} + \ldots.$$

The constant A can be computed theoretically from the outer flow solution as described by Grove, Shair, Petersen & Acrivos (1964). For oblate spheroids, the result, as evaluated by Masliyah, is

$$P_0 = 1 + \frac{8}{R} \frac{\operatorname{sech} \xi_a}{\tau_a^2 \cot^{-1} \lambda_a - \lambda_a}.$$

The above expression is compared with the present numerical work for A.R. = 0·2 in figure 12. The agreement is fairly close for the higher R.

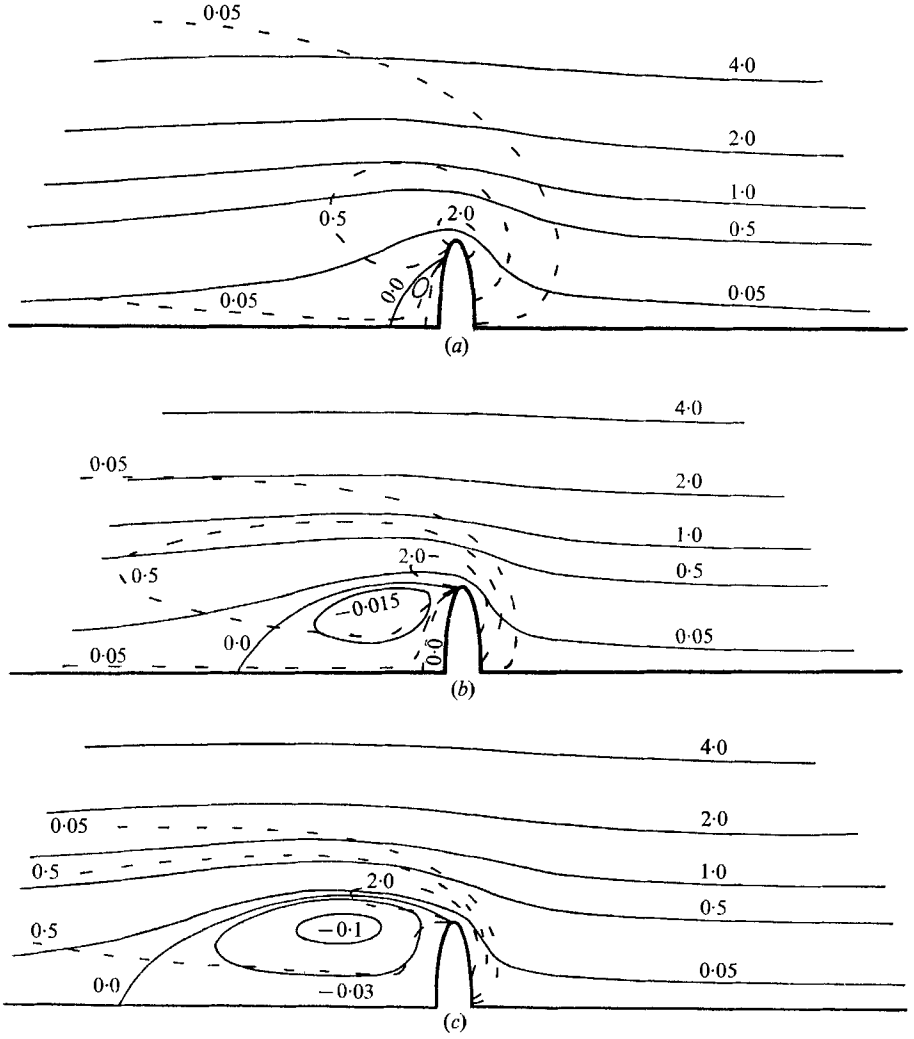

FIGURE 13. Streamlines for oblate spheroids with aspect ratio 0·2; – – – –, vorticity lines. R: (*a*) 10, (*b*) 50, (*c*) 100.

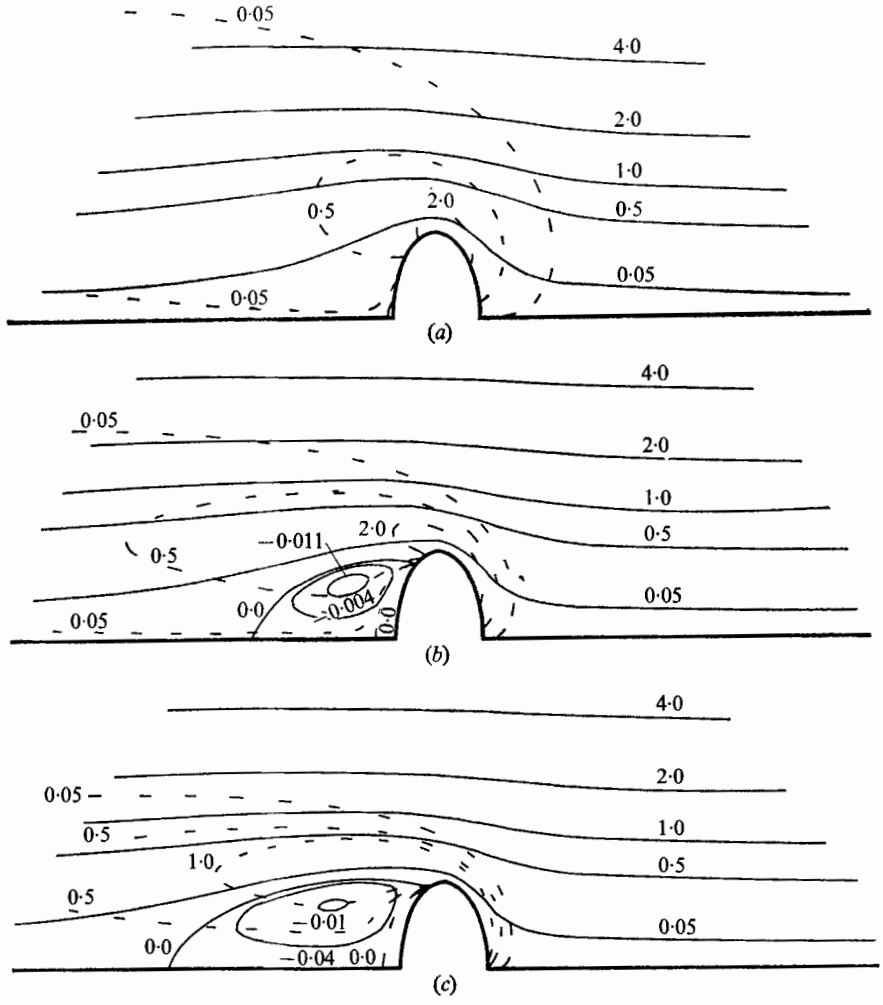

FIGURE 14. Streamlines for oblate spheroids with aspect ratio 0·5; – – –, vorticity lines. R: (*a*) 10, (*b*) 50, (*c*) 100.

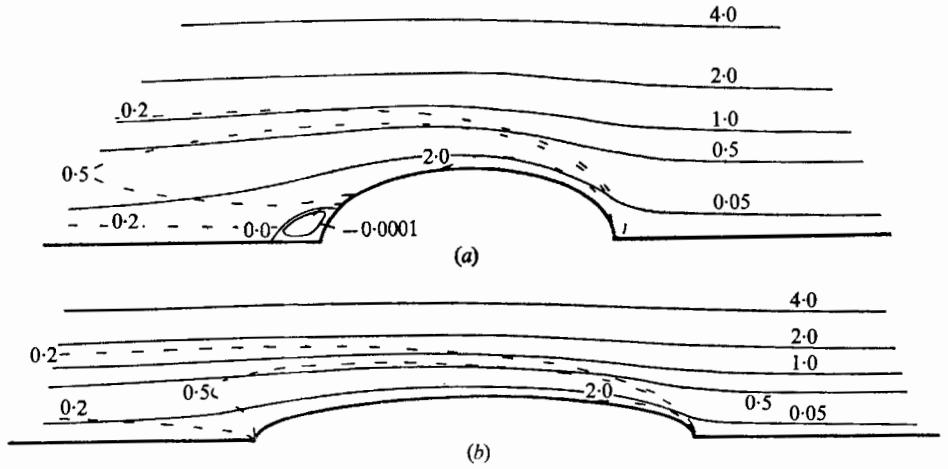

FIGURE 15. Streamlines for prolate spheroids: (*a*) A.R. = 0·5, (*b*) A.R. = 0·2; – – –, vorticity lines. $R = 100$.

The appearance of the wake bubble behind a spheroid is clearly a function of the solid body's shape and of the Reynolds number. It was found that a wake bubble develops for R as low as 20, 10 and 5 for an oblate spheroid with A.R. of 0·9, 0·5 and 0·2, respectively. For an almost spherical oblate spheroid (A.R. = 0·999), this work shows no marked vortex development at $R = 20$,

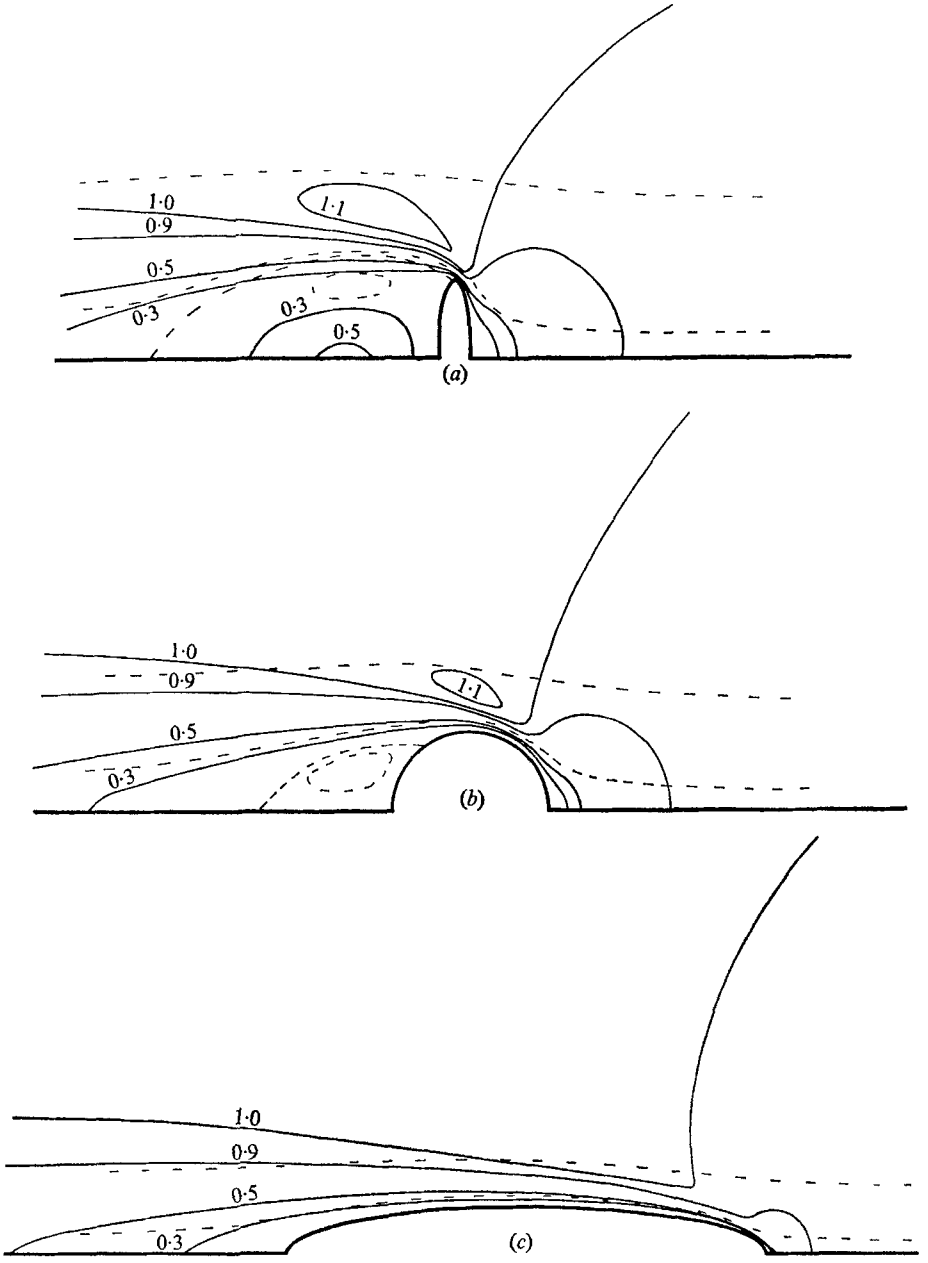

FIGURE 16. Iso-velocity lines for Reynolds number 100; (*a*) oblate spheroid with A.R. = 0·2; (*b*) nearly spherical oblate spheroid (A.R. = 0·999); (*c*) prolate spheroid with A.R. = 0·2. – – –, streamlines.

though a separation was indicated at this R by a negative vorticity at $\eta = 4{\cdot}5°$. At $R = 100$ and A.R. = 0·2 the angle of separation for an oblate spheroid was numerically determined to be 99·7°, in excellent agreement with Rimon & Lugt. For a prolate spheroid of A.R. = 0·2, no vortex was observed even for R of 100.

The deviation of the flow from the Stokes régime, in which symmetry prevails, is best observed by the asymmetry of the vorticity lines, which are a measure of the shear stress at the surface. The vorticity is generated upstream and is carried by the fluid around the spheroid to considerable distances downstream. Streamlines and equi-vorticity lines at various Reynolds numbers and aspect ratios for

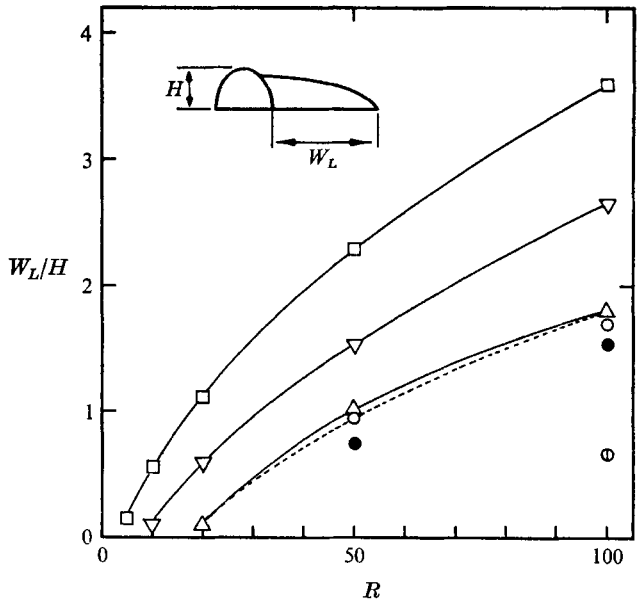

FIGURE 17. Variation of wake length with R for spheroids. Oblate spheroids: □, A.R. = 0·2; ▽, A.R. = 0·5; △, A.R. = 0·9; ○, A.R. = 0·999 (sphere). Prolate spheroids: ●, A.R = 0·9; ⊕, A.R. = 0·5. Sphere: – – –, Van Dyke.

oblate and prolate spheroids are shown in figures 13–15. It is interesting to note that the streamline of magnitude 4.0 tends to be less curved with increasing R, indicating that the flow becomes undisturbed at a shorter distance from the spheroid as R increases. This result correlates with the fact that the wall effect on the drag coefficient decreases with increasing R, as experimentally shown by McNown *et al.* (1948).

The equi-velocity lines at $R = 100$ for both an oblate and a prolate spheroid having an aspect ratio of 0·2, and for an almost spherical oblate spheroid, are shown in figure 16. It is interesting to note that the streamline enclosing the wake for the 0·2 aspect ratio oblate spheroid (figure 16(*a*)) has approximately the same curvature over the wake region as the equi-velocity line of unity, and it may be a conjecture that both lines coincide with each other when the Reynolds number is increased indefinitely. Also, it can be seen that the centre of the vortex lies in a region of low velocity.

The variation of the dimensionless wake length with R is shown in figure 17. It is interesting that Van Dyke's (1964) equation, derived from Oseen's approximation for the wake length behind a sphere, is in excellent agreement with the values of wake length computed for a nearly spherical oblate spheroid (A.R. = 0·999).

The authors are indebted to the University of British Columbia and to the National Research Council of Canada for continuing financial support. Thanks are also due to the U.B.C. Computing Centre for writing the contouring programs of figures 13–16.

REFERENCES

Aoi, T. 1955 *J. Phys. Soc. Japan*, **10**, 119.

Breach, D. R. 1961 *J. Fluid Mech.* **10**, 306.

Folsom, R. G. & Arbor, A. 1956 *Trans. Am. Soc. Mech. Engrs.* **78**, 1447.

Goldstein, S. 1929 *Proc. Roy. Soc.* A, **123**, 216.

Grove, A. S., Shair, F. H., Petersen, E. E. & Acrivos, A. 1964 *J. Fluid Mech.* **19**, 60.

Hamielec, A. E., Hoffman, T. W. & Ross, L. L. 1967 *A.I.Ch.E.J.* **13**, 220.

Happel, J. & Brenner, H. 1965 *Low Reynolds Number Hydrodynamics* (1st edn.). New Jersey: Prentice Hall.

Homann, F. 1936 Der Einfluss grösser Zähigkeit bei der Strömung um den Zylinder und um die Kugel. *Z. angew. Math. Mech.* **6**, 153. (Translation: *NACA Tech. Mem.* 1334, 1952.)

Jenson, V. G. 1959 *Proc. Roy. Soc.* A, **249**, 346.

Jenson, V. G., Horton, J. R. & Wearing, J. R. 1968 *Trans. Inst. Chem. Engrs.* **46**, 177.

Kuwabara, S. 1959 *J. Phys. Soc. Japan*, **14**, 527.

Lapple, C. E. & Shepherd, C. B. 1940 *Ind. Eng. Chem.* **32**, 605.

LeClair, B. P. & Hamielec, A. E. 1968 *Ind. Eng. Chem. Fundamentals*, **7**, 542.

Masliyah, J. H. 1970 Ph.D. Thesis, University of British Columbia.

Masliyah, J. H. & Epstein, N. 1969 *Ind. Eng. Chem. Fundamentals*, **8**, 602.

McNown, J. S., Lee, H. M., McPherson, M. B. & Engez, S. M. 1948 *Proc. VII Int. Congr. Appl. Mech.* **2**, 17.

O'Brien, V. 1961 *Quart. J. Appl. Math.* **19**, 163.

Oseen, C. W. 1910 *Ark. F. Mat. Astr. Og. Fys.* **6**, no. 29.

Oseen, C. W. 1927 *Hydrodynamik*. Leipzig.

Pearcey, T. & McHugh, B. 1955 *Phil. Mag.* (7), **46**, 783.

Proudman, I. & Pearson, J. R. A. 1957 *J. Fluid Mech.* **2**, 237.

Rhodes, J. M. 1967 Ph.D. Thesis, University of Tennessee.

Rimon, Y. & Cheng, S. I. 1969 *Phys. Fluids*, **12**, 949.

Rimon, Y. & Lugt, H. J. 1969 *Phys. Fluids*, **12**, 2465.

Sampson, R. 1891 *Phil. Trans.* **182**, 449.

Schmiedel, J. 1928 *Phys. Z.* **29**, 593.

Stokes, G. 1851 *Trans. Camb. Phil. Soc.* **9**, 8.

Thom, A. 1927 *Aero. Res. Counc. R. & M.* no. 1194.

Tomotika, S. & Aoi, T. 1950 *Quart. J. Mech.* **3**, 140.

Van Dyke, M. D. 1964 *Perturbation Methods in Fluid Mechanics*. New York: Academic.